



Optimization of organic gas sensor performance through sensing area control

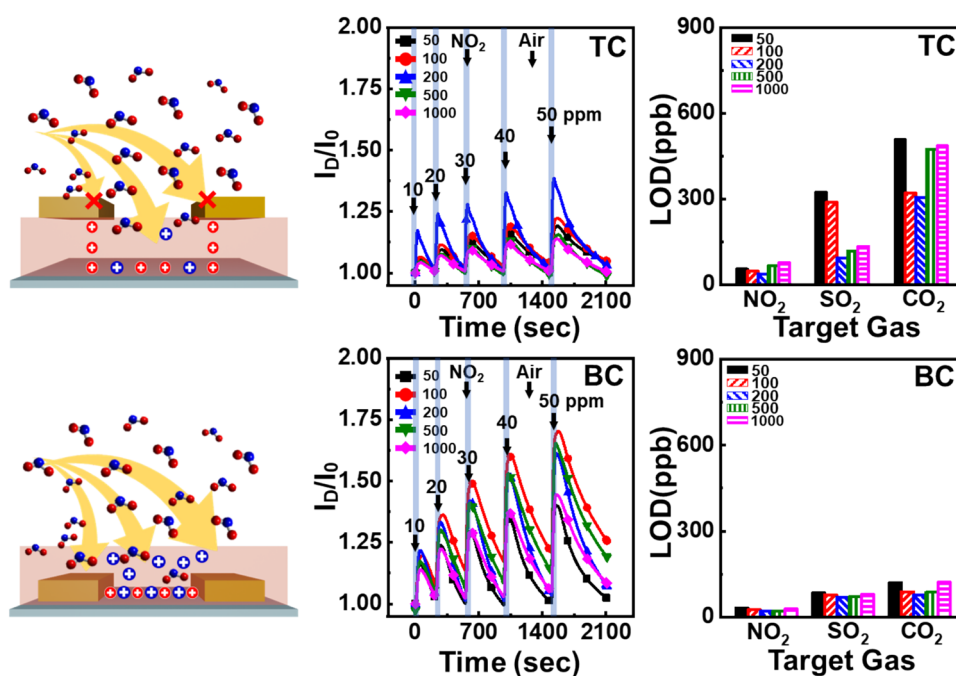
Seunghyeon Jeon¹ · Yeong Don Park^{1,2}

Received: 9 June 2025 / Revised: 30 June 2025 / Accepted: 13 July 2025 / Published online: 23 July 2025
 © The Author(s), under exclusive licence to The Polymer Society of Korea 2025

Abstract

We systematically investigated how contact geometry and channel length affect the gas-sensing performance of organic field-effect transistor (OFET)-based sensors employing poly (3-hexylthiophene) (P3HT) films without any molecular modification or additive doping. Devices with top-contact (TC) and bottom-contact (BC) architectures were fabricated with channel lengths ranging from 50 to 1000 μm . Gas sensing characteristics—including responsivity, sensitivity, and dynamic response behavior—were evaluated upon exposure to nitrogen dioxide. The results revealed that devices with intermediate channel lengths ($\sim 200 \mu\text{m}$) exhibited the highest sensing performance, attributed to an optimal balance between the sensing area available for gas adsorption and the hole carrier diffusion length. Notably, BC gas sensors consistently outperformed their TC counterparts owing to the active layer's improved gas accessibility. This study demonstrates that the gas-sensing area-specific optimization of channel length and device structure can substantially optimize gas-sensing performance, offering a facile and scalable strategy for developing high-performance organic gas sensors.

Graphic abstract



We optimized the gas sensing performance of conjugated polymer-based devices by adjusting the device geometry—specifically channel length and contact structure—without chemical or physical modifications. Notably, the gas sensing area substantially optimizes the gas sensing performance, offering a facile and scalable strategy for developing high-performance organic gas sensors.

Keywords P3HT · OFET · Channel length · Organic gas sensor · Sensing area

1 Introduction

Modern society's rapid progress has fundamentally transformed human lifestyles and industrial frameworks. In response, a variety of next-generation electronic platforms such as wearable devices, sensors, robotics, and smart systems have rapidly emerged [1–5]. These platforms are being investigated for integration into energy-autonomous systems, real-time data acquisition platforms, and environmental monitoring devices across diverse application domains [6–9]. Most high-performance electronic devices in current use are based on silicon-derived inorganic semiconductors, which offer superior charge transport, excellent thermal stability, robust mechanical integrity, and long-term operational reliability. However, inorganic electronic devices are inherently rigid and brittle, exhibit limited optical transparency, and incur high fabrication costs. Consequently, their application in next-generation platforms, such as wearable electronics and flexible sensors for E-skin, which demand mechanical flexibility, optical transparency, and high energy efficiency, remains limited.

Organic electronic materials have emerged as attractive alternatives for overcoming these limitations. Organic semiconductors can be processed at low temperatures and be deposited directly onto flexible substrates via solution processes. Their electrical and mechanical properties can also be customized through molecular design. These materials are lightweight, flexible, and can be transparent under appropriate conditions, making them promising candidates for wearable systems, skin-attachable sensors, and foldable displays [10, 11].

Among the various applications of organic semiconductors, gas sensing is particularly critical for monitoring harmful gases in both environmental and biomedical settings, ensuring human safety and the stable operation of sensitive systems. Reactive gases such as nitrogen dioxide (NO_2), sulfur dioxide (SO_2), and carbon dioxide (CO_2) pose serious health and safety risks even at low concentrations, necessitating sensitive and reliable gas-sensing technologies [12]. Although conventional metal oxide-based gas sensors offer high sensitivity and stable performance, their requirements for high operating temperatures, substantial power consumption, and lack of mechanical flexibility render them unsuitable for portable or wearable applications. To overcome these challenges, organic gas sensors employing conjugated polymers as the active sensing layers have attracted considerable attention. These sensors offer advantages, such as room-temperature operation, low-cost solution

processing, mechanical flexibility, and chemical tunability [13, 14]. Despite these advantages, organic gas sensors still have limitations, e.g., relatively low sensitivity and slow response and recovery times, prompting intensive research into performance enhancement strategies. For example, the chemical modification of conjugated polymers via side-chain engineering has been used to improve gas selectivity and sensitivity. Structural engineering strategies include inducing vertical phase separation to form ultrathin active layers and the selective etching of blended films to generate porous structures. Organic–inorganic hybrid materials that incorporate nanoporous materials such as metal–organic frameworks or carbon-based nanostructures have also been explored. Additionally, surface functionalization techniques such as UV–ozone treatment or the introduction of self-assembled monolayers on silica surfaces have been employed to improve gas adsorption and transport [15–22]. Despite their effectiveness, these methods often involve complex synthesis, poor film uniformity, and multistep fabrication processes, which hinder their scalability and practical implementation.

This study demonstrates that simply modulating the channel length and contact geometry in a poly (3-hexylthiophene) (P3HT) based field-effect transistor can significantly enhance the gas-sensing performance without physical and chemical modification or blending porous materials. Our results reveal that while a short channel is typically advantageous for conventional transistor performance, it may diminish the gas-sensing capability by reducing the effective gas adsorption area. These findings highlight the critical role of device structural design in gas sensors and suggest that even simple geometric tuning can be an effective and scalable strategy that enhances the sensing performance and provides a robust platform for future integration with advanced functional materials.

2 Experimental

2.1 Fabrication and characterization of the P3HT thin film

P3HT with molecular characteristics of ($M_n = 58$ kDa, regioregularity = 96%, $2.0 \leq \text{PDI} \leq 2.3$) was purchased from Rieke Metals and used as received without further purification. P3HT is a p-type-conjugated polymer widely employed as an active material in organic electronic devices. Highly n-doped silicon wafers ($2\text{ cm} \times 2\text{ cm}$) with a 3000 Å

thermally grown SiO₂ layer were used as substrates. To remove the organic contaminants, the substrates were sequentially sonicated in acetone and ethanol for 30 min. After cleaning, the wafers were exposed to UV-ozone for 40 min to enhance surface reactivity further. Subsequently, surface modification was carried out by spin-coating hexamethyldisilazane (HMDS) at 2500 rpm for 30 s, followed by baking at 125 °C for 1 h. The P3HT was dissolved in chloroform at a concentration of 5 mg/mL. The solution was stirred and heated at 50 °C for 1 h to ensure complete dissolution, then cooled to room temperature prior to deposition. The prepared P3HT solution was spin-coated onto the HMDS-treated SiO₂/Si substrates at 2000 rpm for 60 s to form uniformly thin films. The resulting P3HT films were characterized using UV–Vis spectrophotometry (Lambda 365, PerkinElmer) to investigate their molecular orientation and crystallinity. The surface morphology was analyzed by atomic force microscopy (AFM, Multimode 8, Bruker). Thickness of the P3HT film from the UV–Vis absorption spectra using Beer's law. Beer's law provides a relationship among absorbance, molar extinction coefficient (ϵ), path length (l) and concentration (c):

$$A = \epsilon lc$$

2.2 Fabrication of OFETs and gas sensors

Organic field-effect transistors (OFETs) and gas sensors were fabricated using spin-coated P3HT thin films. Top-contact (TC) and bottom-contact (BC) architectures were fabricated using shadow masks with a fixed channel width of 2000 μm and varying channel lengths of 50, 100, 200, 500, and 1000 μm . For the TC type devices, 100 nm of Au was thermally evaporated to form source and drain electrodes on the P3HT film. For the BC type devices, a 5 nm Ti adhesion layer was first deposited, followed by a 100 nm Au layer. The P3HT active layer was then fabricated by spin-coating the Au electrodes for BC. The fabricated OFET and gas sensors were integrated into an external measurement system by connecting silver paste and wires to the electrodes, enabling both electrical characterization and gas-sensing performance evaluation.

2.3 Characterization of OFETs and gas sensors

The charge transport characteristics of the OFETs were analyzed under vacuum and room-temperature conditions using a semiconductor analyzer (Keithley 4200-SCS). The drain–source current (I_D) was measured at a constant drain voltage of -60 V, with the gate voltage swept from -60 V to 60 V. Field-effect mobility values were extracted from the transfer characteristics within the gate voltage range of -30 V

to -60 V. The field-effect mobility in saturated regime (μ_{FET}) was calculated using the following equation:

$$I_D = \frac{W}{2L} C_i \mu_{\text{FET}} (V_G - V_{th})^2.$$

Gas sensing characteristics were evaluated using a gas sensor tester (GASENTEST II) and semiconductor analyzer (Keithley 2636B) at gate and drain voltages of -20 V. High-purity calibration gas cylinders ($\geq 99.9\%$), including balance air, were supplied by RIGAS, Korea to ensure reproducibility and accuracy. During the experiments, the target gas was introduced into a sealed reaction chamber at concentrations ranging from 10 to 50 ppm. Following exposure cycles, balance air was used to purge the chamber, ensuring sensor recovery and consistent baseline conditions for subsequent cycles.

2.4 Calculation of gas-sensing parameters

The responsivity (R) was calculated based on repeated exposure experiments using 10 ppm of NO₂ gas, under a representative low-concentration condition to evaluate the reproducibility and stability of the sensor response. The calculation used the following equation:

$$R = \left| \frac{I_D - I_0}{I_0} \right|,$$

where (I_0) is the drain current under ambient air (baseline) conditions, and (I_D) is the drain current upon exposure to the target gas. The response and recovery rates were determined from the time-dependent normalized current response and were calculated using the following equations:

$$\text{Rate} = \frac{\Delta(I_D - I_0)}{\Delta T}.$$

These rates quantify the speed of the sensor response and return to baseline upon gas exposure and removal, respectively. The sensitivity (S) was determined by calculating the derivative of R regarding the gas concentration, as expressed by the following equation:

$$S = \frac{\partial R}{\partial C_t},$$

where R denotes the responsivity obtained from the dynamic sensing tests at each gas concentration, and C_t represents the concentration of the target gas.

3 Results and discussion

3.1 P3HT thin film morphology

The structural and morphological properties of the spin-coated P3HT thin films were analyzed using UV–Vis absorption spectroscopy and atomic force microscopy (AFM). The UV–Vis absorption spectrum of the P3HT film presented in Fig. 1a exhibits distinct vibronic features. The A_{0-2} peak at 524 nm corresponds to the intrachain $\pi-\pi^*$ transition, while the A_{0-1} and A_{0-0} peaks at 556 nm and 605 nm, respectively, are attributed to interchain $\pi-\pi$ interactions. The film thickness, calculated using Beer's law from the UV–Vis absorption data, was approximately 30 nm, as shown in Fig. 1b.

AFM analysis confirmed that the P3HT film surface on the HMDS-treated SiO_2 dielectric and Au electrode are uniform with well-distributed nanostructures. Height and phase images in Fig. 1c and d reveal a continuous film with very low surface roughness and a subtle nanoscale texture. Due to the difference in surface energy and surface roughness between the SiO_2 and Au electrode, the RMS roughness of P3HT film slightly increased from 1.37 nm on SiO_2 to 1.87 nm on Au (Fig. 1c).

3.2 OFET performance

Figure 2 presents the transfer characteristics of OFETs including channel lengths and contact geometry. The on-current level gradually decreases with a longer channel length,

gradually reducing the on/off current ratio. In contrast, the field-effect mobility remains nearly constant, irrespective of the channel length and contact configuration (Table 1). BC OFETs with a channel length of 50 μm showed lower field-effect mobility because high contact resistance accounts for a large proportion of the total resistance. Overall, OFETs presented relatively similar field-effect mobility regardless of the device structure, because OFETs have long channel length and the morphology and structure of the active layer on the electrodes and channel regions are similar [23, 24].

3.3 Gas sensing performance

To evaluate the sensing performance of the gas sensor with the proposed channel length and contact configuration, the source–drain current was monitored at room temperature (Fig. 3). The TC and BC gas sensors with various channel lengths are shown in Fig. 3a and e, respectively. P3HT thin films were exposed to 10 ppm of NO_2 for 20 s, followed by 200 s of air purging. Figure 3b and f shows the sensing responses of TC and BC OFETs, respectively. All measurements were performed at a fixed drain voltage (V_D) and gate voltage (V_G) of -20 V.

The first sensing cycles of the TC and BC gas sensors are shown in Fig. 3c and g, respectively, from which the key performance parameters were extracted and are summarized in Fig. 3d and h. In both TC and BC OFETs, sensing performance was improved as the channel length increased from 50 μm to 200 μm . This trend is attributed to the increased sensing area, which facilitates enhanced gas adsorption during the exposure period. Accordingly, as the channel length increased, the gas sensor simultaneously exhibited improved responsivity and faster response and recovery rates. However, a gas sensor with a channel length of 500 μm or more exhibited deteriorated sensing performance. A long channel length decreases the sensing performance owing to the long-distance hole transport, despite an expanded sensing area.

The BC OFETs consistently exhibited superior gas-sensing performance compared to the TC OFETs (Fig. 3d–e). To investigate further the dynamic sensing at various gas concentrations, the NO_2 level was increased from 10 ppm to 50 ppm (Fig. 4). As the NO_2 concentration increased, a proportional increase in drain current was observed (Fig. 4, panels a and d). Consistent with previous results, the gas sensor with a 200 μm channel showed the highest performance regardless of the contact configuration, and the BC gas sensor showed overall high sensing performance compared to the TC gas sensor. This superior sensing performance was attributed to the large gas-exposure area in the BC OFET structure. The architectural advantages of BC gas sensors allow the more efficient adsorption and desorption of gas molecules across the active-layer film channels.

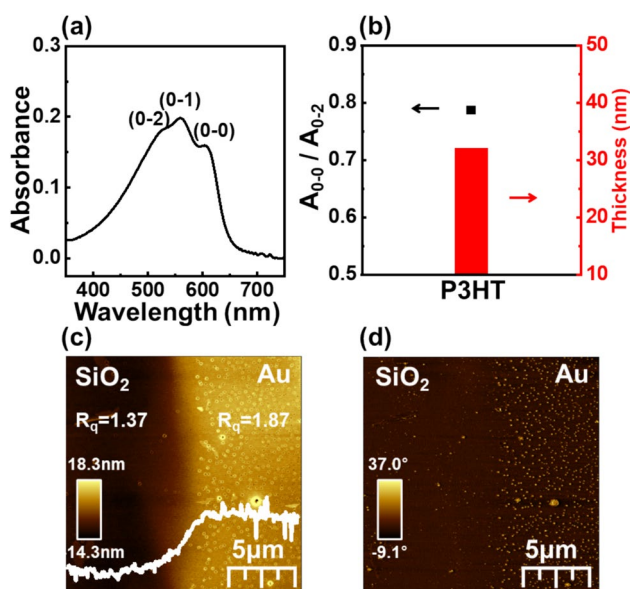


Fig. 1 **a** UV–Vis absorption spectrum of P3HT film, **b** calculated molecular order and film thickness. AFM **c** Z-axis height and **d** phase images of P3HT films on SiO_2 and Au electrodes

Fig. 2 Transfer characteristics (I_D vs V_G at $V_D = -60$ V) with **a** TC and **c** BC OFETs, field-effect mobility (left axis), and on/off ratio (right axis) with **b** TC and **d** BC OFETs, and **e** an illustration of TC (left) and BC (right) OFETs

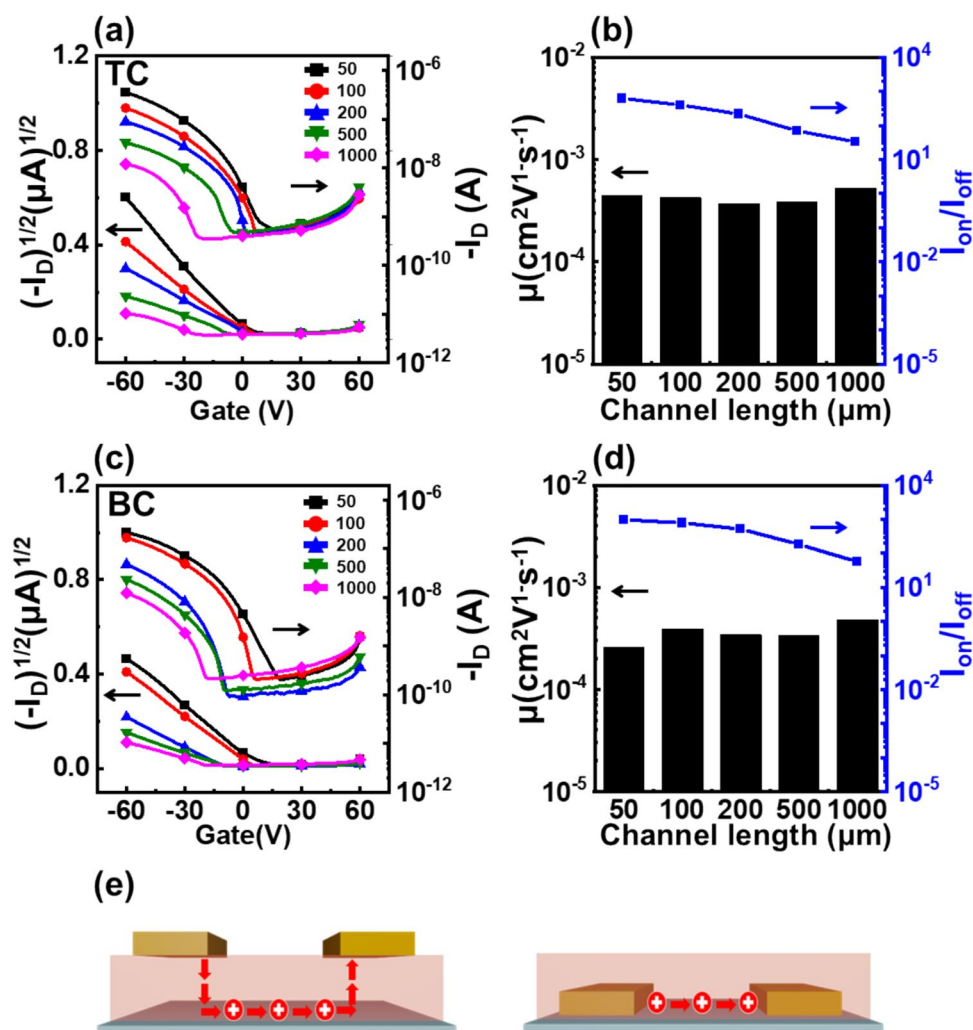


Table 1 Field-effect mobility and on/off ratio of OFETs with channel lengths and contact configurations

Channel length (μm)	Field-effect mobility ($\times 10^{-3} cm^2/Vs$)		On/off ratio ($\times 10^2$)	
	TC	BC	TC	BC
50	0.45	0.26	6.25	9.74
100	0.43	0.39	4.00	7.82
200	0.37	0.34	2.19	5.22
500	0.39	0.34	0.70	1.83
1000	0.53	0.48	0.33	0.56

In practical environments, gas sensors are frequently exposed to various gas species. The reliable detection of a specific target gas necessitates a markedly stronger sensor response to the target gas relative to the potential interference with other analytes. To assess this essential aspect of selectivity, the additional sensing experiments shown in Fig. 5 were subsequently conducted for SO_2 and CO_2 .

Sensitivity increases with channel lengths up to 200 μm and subsequently decreases while gas sensors with BC architectures consistently demonstrate higher sensitivities than those with TC configurations. An enlarged sensing area in BC architectures can enhance the sensing performance, even for analytes that exhibit inherently lower reactivity. This enhancement is attributed to the increased adsorption capacity enabled by the BC structure, which facilitates more efficient gas penetration and charge transport, thereby yielding superior sensing performance.

The limit of detection (LOD) is a key parameter for evaluating the performance of gas sensors. The theoretical LOD was calculated from the measured results. According to the International Union of Pure and Applied Chemistry, LOD is the lowest concentration of analyte that provides a signal three times the noise level [25]. The noise level of the sensor was determined by calculating the root mean square deviation. The root mean square noise (RMS_{noise}) was estimated from ten randomly selected data points in the linear baseline region of the current–time response

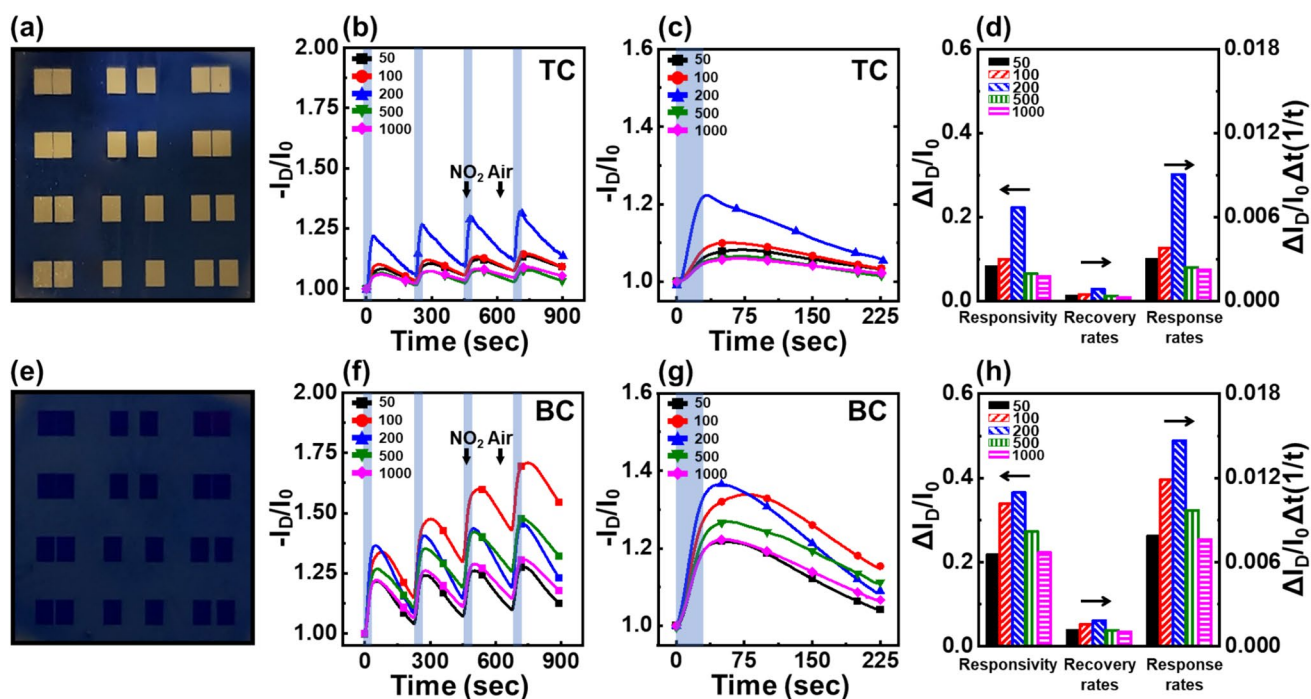
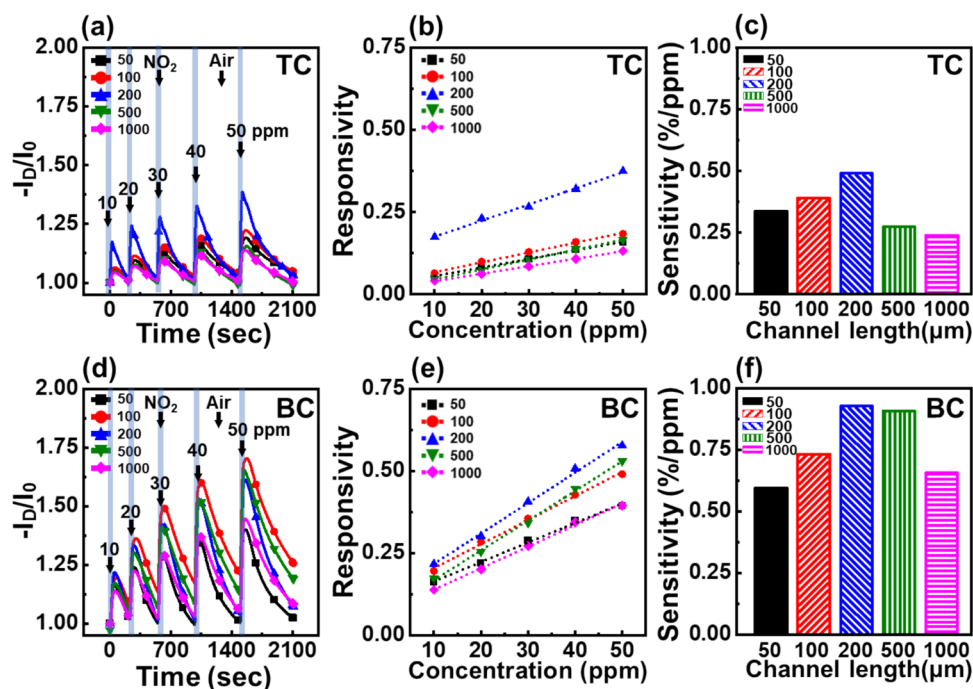


Fig. 3 Photographs of **a** TC and **e** BC gas sensors showing channel lengths. Normalized drain current responses to 10 ppm NO_2 exposure for **b** TC and **f** BC gas sensors, and their first sensing cycles in **c** TC

and **g** BC gas sensors. Summary of gas-sensing parameters, including responsivity, response rate, and recovery rate in **d** TC and **h** BC gas sensors

Fig. 4 Normalized drain current responses to NO_2 concentrations ranging from 10 to 50 ppm for **a** TC and **d** BC gas sensor. Responsivity vs gas concentration for **b** TC and **e** BC gas sensors, and calculated sensitivity values for **c** TC and **f** BC gas sensors



curve prior to gas exposure. Fifth-order polynomial fitting was applied to model the baseline current behavior, and the $\text{RMS}_{\text{noise}}$ was calculated using the following equation: [26]

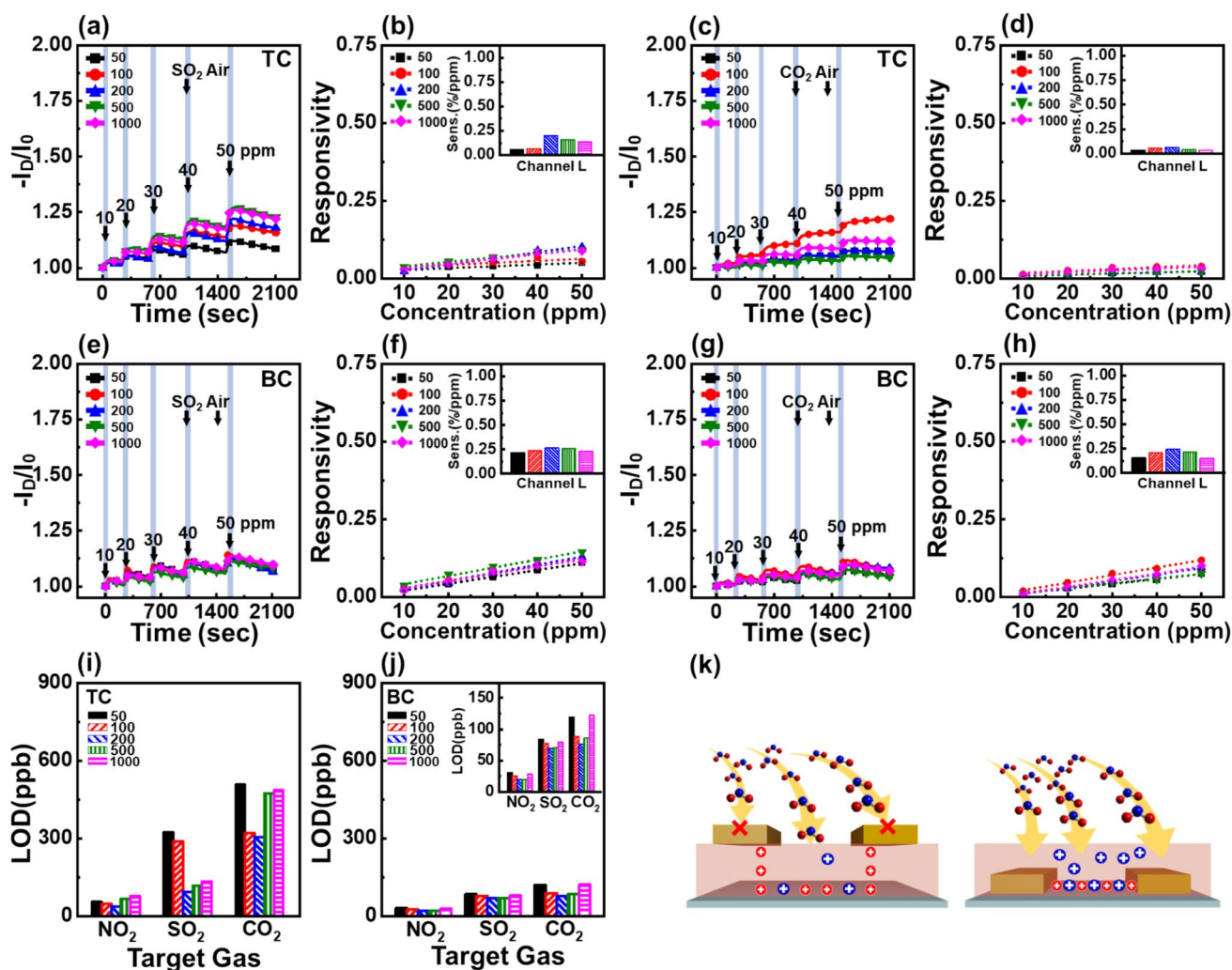


Fig. 5 Dynamic sensing responses of TC gas sensors for **a** SO₂ and **c** CO₂ gases. Dynamic sensing responses of BC gas sensors for **e** SO₂ and **g** CO₂. Responsivity vs concentration and sensitivity (inset) for TC gas sensors for **b** SO₂ and **d** CO₂; corresponding plots for BC gas

sensors shown in **(f)** and **(h)**. Calculated LOD versus channel length with **i** TC gas sensors and **j** BC gas sensors (inset shows enlarged LOD of BC). **k** Schematic of the gas adsorption mechanism based on device structure

$$RMS_{noise} = \sqrt{\frac{\sum_{i=1}^N (Y_i - Y)^2}{N}},$$

where N is the number of data points, Y_i is the experimentally measured current, and Y is the value obtained from the polynomial fit. The LOD values were estimated using the calculated RMS_{noise} and are summarized in Fig. 5i and j. The results show that the TC gas sensor exhibited LODs in the sub-ppm range, whereas the BC gas sensor achieved LODs below 100 ppb. A comparative analysis of the minimum detectable NO₂ concentration revealed that the best-performing BC gas sensor exhibited an approximately 2.75 times lower LOD than the TC gas sensor.

The gas-sensing mechanism is primarily governed by the interaction between NO₂ molecules and the active layer.

As an electron-withdrawing oxidizing gas, NO₂ captures electrons from the P3HT polymer backbone, enhancing hole accumulation and causing drain current to increase [27, 28]. The channel length strongly influences this p-type sensing behavior. As the channel length increases, the area exposed to the gas expands, allowing more molecules to interact with the active layer, thereby producing a stronger response. However, excessive increases in the channel length can degrade the overall current levels of OFETs, leading to diminished sensing capability despite the enlarged sensing area.

The sensing performance is also affected by the device structure. In TC gas sensors, electrodes partially block gas adsorption onto the channel, thereby limiting the gas molecules' penetration into the active layer. In contrast, BC gas sensors have electrodes located beneath the active layer,

which allows gas molecules to reach the channel region more effectively. As schematically shown in Fig. 5k This structural advantage promotes a more accessible gas diffusion pathway and contributes to the superior sensing performance consistently observed in BC gas sensors. These findings highlight that selecting the appropriate device structure and channel length is critical for optimizing sensor performance.

4 Conclusions

This study successfully investigated the sensing performance of organic gas sensors with different channel lengths and device structures. Our results demonstrated that the optimized condition—a BC gas sensor with a 200 μm channel length—exhibited sensing performance up to five times that of a TC gas sensor with a short channel length. These findings underscore the importance of the sensing area at the device level and suggest that even simple geometric tuning can significantly improve gas-sensing performance. This approach provides a foundation for developing high-performance, low-cost organic gas sensors and may serve as a platform for the future integration of functional nanomaterials to further enhance sensitivity.

Acknowledgements This work was supported by the National Research Foundation of Korea (NRF) grant funded by the Korea government (MSIT) (No. NRF-2023R1A2C1005218).

Funding The National Research Foundation of Korea (NRF) grant funded by the Korea government (MSIT), NRF-2023R1A2C1005218, Yeong Don Park.

Declarations

Conflict of interest The authors declare that they have no known competing financial interests or personal relationships that could have appeared to influence the work reported in this paper.


References

1. H. Park, J. Han, S. Myoung, M. Kim, H. Lim, D. Kim, G. Lee, *Macromol. Res.* (2025). <https://doi.org/10.1007/s13233-025-00384-9>
2. J.J. Kim, Y. Wang, H. Wang, S. Lee, T. Yokota, T. Someya, *Adv. Funct. Mater.* **31**, 2009602 (2021)
3. S. Qazi, B.A. Khawaja, Q.U. Farooq, *IEEE Access* **10**, 21219–21235 (2022)
4. W. Li, Y. Chai, F. Khan, S.R.U. Jan, S. Verma, V.G. Menon, F. Kavita, X. Li, *Mobile Netw. Appl.* **26**, 234–252 (2021)
5. Z. Liu, Q. Liu, W. Xu, L. Wang, Z. Zhou, *Robot. Comput.-Integr. Manuf.* **77**, 102360 (2022)
6. L. Manjakkal, L. Yin, A. Nathan, J. Wang, R. Dahiya, *Adv. Mater.* **33**, 2100899 (2021)
7. J. Yi, G. Zhang, H. Yu, H. Yan, *Nat. Rev. Mater.* **9**, 46–62 (2024)
8. M.S. Park, M.J. Kim, J.Y. Jeong, D.Y. Han, S. Kim, G.-T. Hwang, H. Yoo, E.K. Lee, *Macromol. Res.* **33**, 451–461 (2025)
9. J. Kim, H. Jung, M. Kim, H. Bae, Y. Lee, *Macromol. Res.* **29**, 761–775 (2021)
10. X. Xu, Y. Zhao, Y. Liu, *Small* **19**, 2206309 (2023)
11. Z. Mei, L.A. Deng, B. Huang, W. Tang, X. Guo, *IEEE J. Flex. Electron.* **3**(11), 508–521 (2018)
12. S. Dhall, B. Mehta, A. Tyagi, K. Sood, *Sens. Int.* **2**, 100116 (2021)
13. I.H. Ko, Y.D. Park, A.C.S. Appl. Polym. Mater. **7**(5), 2749–2760 (2025)
14. N. Gu, Y.D. Park, *Polym. Korea* **48**(6), 576–585 (2024)
15. J. Hwang, J. Shin, W.H. Lee, *Macromol. Res.* **33**, 1–14 (2024)
16. X. Wang, Z. Liu, S. Wei, F. Ge, L. Liu, G. Zhang, Y. Ding, L. Qiu, *Synth. Met.* **244**, 20–26 (2018)
17. V.V. Tran, G. Jeong, K.S. Kim, J. Kim, H.-R. Jung, B. Park, J.-J. Park, M. Chang, *ACS Sens.* **7**(1), 175–185 (2021)
18. G. Jeong, H.J. Cheon, S.Y. Shin, E. Wi, P. Kyokunzire, H. Cheon, V. Van Tran, T.T. Vu, M. Chang, *Dyes Pigment.* **214**, 111235 (2023)
19. S. Yuvaraja, S.G. Surya, V. Chernikova, M.T. Vijjapu, O. Shehah, P.M. Bhatt, S. Chandra, M. Eddaoudi, K.N. Salama, A.C.S. Appl. Mater. Interfaces. **12**(16), 18748–18760 (2020)
20. Y.E. Hahm, S. Kweon, M.B. Park, Y.D. Park, A.C.S. Appl. Mater. Interfaces **15**(5), 7196–7203 (2023)
21. W. Huang, X. Zhuang, F.S. Melkonyan, B. Wang, L. Zeng, G. Wang, S. Han, M.J. Bedzyk, J. Yu, T.J. Marks, *Adv. Mater.* **29**, 1701706 (2017)
22. Y.E. Hahm, B.H. Park, S.Y. Park, T.K. An, J. Lee, Y.D. Park, *Org. Electron.* **104**, 106493 (2022)
23. Y. Chen, I. Shih, *J. Mater. Sci.* **44**, 280–284 (2009)
24. Y. Xu, W. Scheideler, C. Liu, F. Balestra, G. Ghibaudo, K. Tsukagoshi, *IEEE Electron Device Lett.* **34**(4), 535–537 (2013)
25. L.A. Currie, *Pure Appl. Chem.* **67**(10), 1699–1723 (1995)
26. Y. Zhou, G. Liu, X. Zhu, Y. Guo, *Sens. Actuator B-Chem.* **251**, 280–290 (2017)
27. S. Yuvaraja, A. Nawaz, Q. Liu, D. Dubal, S.G. Surya, K.N. Salama, P. Sonar, *Chem. Soc. Rev.* **49**, 3423–3460 (2020)
28. S. Zhao, S. Hou, H. Fan, Z. Wang, J. Yu, *Synth. Met.* **269**, 116569 (2020)

Publisher's Note Springer Nature remains neutral with regard to jurisdictional claims in published maps and institutional affiliations.

Springer Nature or its licensor (e.g. a society or other partner) holds exclusive rights to this article under a publishing agreement with the author(s) or other rightsholder(s); author self-archiving of the accepted manuscript version of this article is solely governed by the terms of such publishing agreement and applicable law.

Authors and Affiliations

Seunghyeon Jeon¹ · Yeong Don Park^{1,2} 

✉ Yeong Don Park
ydpark@inu.ac.kr

² Innovation Center for Chemical Engineering, Incheon
National University, Incheon 22012, Republic of Korea

¹ Department of Energy and Chemical Engineering, Incheon
National University, Incheon 22012, Republic of Korea